HIGHLY STRUCTURED INNER PLANETARY SYSTEM DEBRIS AROUND THE INTERMEDIATE AGE SUN-LIKE STAR TYC 8830 410 1

Carl Melis

email: cmelis@ucsd.edu
Center for Astrophysics and Space Sciences, University of California, San Diego, CA 92093-0424, USA

Johan Olofsson

Instituto de Física y Astronomía, Facultad de Ciencias, Universidad de Valparaíso, Av. Gran Bretaña 1111, Playa Ancha, Valparaíso, Chile
and Núcleo Milenio de Formación Planetaria (NPF), Chile

Inseok Song

Department of Physics and Astronomy, University of Georgia, Athens, GA 30602-2451, USA

Paula Sarkis

Max-Planck-Institut für Astronomie, Königstuhl 17, Heidelberg 69117, Germany

Alycia J. Weinberger

Earth and Planets Laboratory, Carnegie Institution for Science, 5241 Broad Branch Rd NW, Washington, DC 20015, USA

Grant Kennedy

Department of Physics, University of Warwick, Gibbet Hill Road, Coventry CV4 7AL, UK

Mirko Krumpe

Leibniz-Institut für Astrophysik Potsdam (AIP), An der Sternwarte 16, 14482 Potsdam, Germany

ABSTRACT

We present detailed characterization of the extremely dusty main sequence star TYC 8830 410 1. This system hosts inner planetary system dust ($T_{\rm dust} \approx 300\,$K) with a fractional infrared luminosity of $\sim$1%. Mid-infrared spectroscopy reveals a strong, mildly-crystalline solid-state emission feature. TYC 8830 410 1 (spectral type G9 V) has a 49.5$''$ separation M4-type companion co-moving and co-distant with it, and we estimate a system age of $\sim$600 Myr. TYC 8830 410 1 also experiences "dipper"-like dimming events as detected by ASAS-SN, *TESS*, and characterized in more detail with the LCOGT. These recurring eclipses suggest at least one roughly star-sized cloud of dust orbits the star in addition to assorted smaller dust structures. The extreme properties of the material orbiting TYC 8830 410 1 point to dramatic dust-production mechanisms that likely included something similar to the giant-impact event thought to have formed the Earth-Moon system, although hundreds of millions of years after such processes are thought to have concluded in the solar system. TYC 8830 410 1 holds promise to deliver significant advances in our understanding of the origin, structure, and evolution of extremely dusty inner planetary systems.

1. INTRODUCTION

Infrared observations of main sequence stars have demonstrated the existence of exceptionally dusty inner planetary systems. This is defined here to mean those stars hosting infrared excess emission having fractional infrared luminosity (τ=L_{IR}/L_{bol}) of $\gtrsim 1\%$ for dust populations characterized by blackbody emission with an effective temperature of $T_{dust} \gtrsim 300$ K. These are the dustiest main sequence stars known and such systems are exceedingly rare (e.g., Uzpen *et al.* 2009; Balog *et al.* 2009; Melis *et al.* 2010; Kennedy & Wyatt 2013). To date, only a handful are known that have such high levels of mid-infrared excess emission and hence inner planetary system dust (see e.g., Gorlova *et al.* 2004; Song *et al.* 2005; Gorlova *et al.* 2007; Rhee *et al.* 2007; Rhee *et al.* 2008; Melis *et al.* 2010; Zuckerman *et al.* 2012; Melis *et al.* 2012; Schneider *et al.* 2013; Melis *et al.* 2013; Gaidos *et al.* 2019; Tajiri *et al.* 2020; Moór *et al.* 2021). Although it seems reasonably settled that transient collisional events between rocky bodies are necessary to generate the exceptionally dusty disks (Wyatt 2008; Fujiwara *et al.* 2012a; Olofsson *et al.* 2012), it is not clear if the dust is generated in a specific star- or planet-formation event or how it might impact fully-formed planets (Melis 2016; Kral *et al.* 2017; Moór *et al.* 2021).

Some extremely dusty main sequence systems have recently been found to additionally exhibit dimming events due to the passage of circumstellar material along our line of sight (e.g., de Wit *et al.* 2013; Kennedy *et al.* 2017; Gaidos *et al.* 2019; Tajiri *et al.* 2020). These are similar in lightcurve behavior to the "dipper" behavior seen for protoplanetary disk systems (e.g., Morales-Calderón *et al.* 2011; Cody *et al.* 2014, and references therein), although their circumstellar material is thought to be secondary in nature (generated by the collisional breakdown of mature planetesimals/planets). Such systems are typically young ($\lesssim 100$ Myr) and in at least one case are also host to gaseous material (e.g., Punzi *et al.* 2018).

Main sequence systems with both strong infrared excess emission from inner planetary system dust and "dipper" behavior can provide unique insight into the structure and evolution of this material (e.g., Kennedy *et al.* 2017; Gaidos *et al.* 2019). Infrared excess emission provides the means to localize (to some extent) the dust in the planetary system (avoiding potentially confounding situations like in the cases of J140747.93−394542.6, KIC 8462852, or similar stars; Mamajek *et al.* 2012; Boyajian *et al.* 2016, 2018; Meng *et al.* 2017; David *et al.* 2017; Mentel *et al.* 2018; Ansdell *et al.* 2019; Rappaport *et al.* 2019; Saito *et al.* 2019) while occultations in the lightcurve provide detailed information on its opacity and spatial organization (e.g., van Werkhoven *et al.* 2014; Kenworthy & Mamajek 2015; Kennedy *et al.* 2017).

In this paper we present the discovery of the oldest (~ 600 Myr) extremely dusty main sequence star to also host dimming events due to orbiting material.

2. LITERATURE SUMMARY

TYC 8830 410 1 was first discovered to be an infrared excess star in the survey of Cotten & Song (2016). They suggest an uncertain spectral type of K3 (stellar T_{eff} of 4900 K), blackbody-fit dust temperature of 425 K and associated orbital radius of 0.2 AU for blackbody-emitting grains, and a fractional infrared luminosity of 1.2%. Subsequent works also found TYC 8830 410 1 to be an excess star (e.g., Marton *et al.* 2016; McDonald *et al.* 2017), but no further characterization of the excess was presented.

Optical spectroscopy of TYC 8830 410 1 was conducted as part of the RAVE survey (Kunder *et al.* 2017). From observations made on 2009-11-10 (MJD of 55145.39994213) they measured a heliocentric radial velocity of 7.0 ± 1.8 km s^{-1}, stellar T_{eff} of 5350 ± 140 K, stellar gravity $\log g$ of 4.4 ± 0.3 in cgs,

and metallicity [M/H] of -0.1 ± 0.2. Further analysis on the RAVE spectra by Žerjal *et al.* (2017) suggested the presence of chromospheric Ca II infrared triplet emission from which an age of $\approx$370 Myr is estimated.

TYC 8830 410 1 has appeared in every *Gaia* release. We adopt parameters measured for it from DR2 and EDR3 (Gaia Collaboration *et al.* 2018, 2020); these are displayed in Table 1. While investigating the *Gaia* data, we identified a co-moving wide-separation companion to TYC 8830 410 1. We describe this object in Section 4.1.

3. OBSERVATIONS

In this section we describe observations obtained for this work and archival data analyzed for this system for the first time.

3.1. FEROS

Multiple epochs of optical echelle spectroscopy were obtained for TYC 8830 410 1 with FEROS at the MPG/ESO 2.2 m telescope at La Silla Observatory (Kaufer *et al.* 1999). Observations were conducted in the "Object-Calibration" mode with one fiber obtaining a simultaneous ThAr lamp spectrum to produce precise ($\lesssim$20 m s^{-1}) radial velocities to aid in searching for close-separation companions.

Data are reduced with CERES (Brahm *et al.* 2017), which also produces precision radial velocities for each epoch and associated uncertainties. FEROS observation epochs and measured velocities are listed in Table 2 along with literature velocities.

3.2. MagE

Observations with MagE at Magellan/Baade were obtained for the wide-separation companion on UT 10 November 2019. The spectrograph was used with a 0.5$''$ slit resulting in R$\sim$8,000 spectra from 4100-10600 Å. Data are reduced with the facility Carnegie Python pipeline (Kelson *et al.* 2000; Kelson 2003). A total integration time of 2700 seconds resulted in a signal-to-noise ratio of 40 per pixel near Hα, 50 per pixel near Li I λ6708, and >50 per pixel in the TiO bands at 7000-7600 Å. Two RV and spectral type standard stars were also observed with the same setup: GJ 54.1 in a 60 second integration and GJ 908 in a 10 second integration.

3.3. VISIR

Mid-infrared imaging and spectroscopy were obtained with the VISIR instrument (Lagage *et al.* 2004; Käufl *et al.* 2015) mounted on VLT-Melipal at Paranal Observatory. Observations were conducted in service mode.

Imaging observations were conducted on UT 04 January 2016 in the AutoChopNod mode with default parameters, the chop/nod direction set to perpendicular, and positioning of the source in the left half of the chip. The 1024 × 1024 pixel detector was configured for 0.045$''$ pixel^{-1} yielding a field of view of roughly 46$''$ × 46$''$. Observations were performed with the PAH1 filter (8.59 μm central wavelength and a half-band width of 0.42 μm) and exposed for a total of 2440 seconds on source. The flux standard HD 220440 (Cohen *et al.* 1999) was observed immediately after observations of TYC 8830 410 1.

Spectroscopic observations were conducted over four nights in late September/early October 2016. Each visit typically consisted of observations of TYC 8830 410 1 and two calibration stars (one before and one after observation of the science target), spending $\approx$90 minutes total wall clock time on the science target. The detector was configured for low-resolution spectroscopy and yielded a 0.076$''$ pixel^{-1} spatial scale and spectral resolving power of R$\sim$300 from 7.5-14 μm with the N-band prism and 0.75$''$ slit. Sources were nodded along the slit with a 10$''$ throw to cancel out background emission and structure.

Data reduction was performed with in-house IDL routines optimized for background-limited observations. In brief, two-dimensional images were chop- and nod-differenced and combined for both the standard stars and the science target. Flux was extracted for each positive and negative beam for all targets with an aperture that yielded approximately 85% encircled energy.

For imaging data, each of the four chop/nod beams were averaged and the uncertainty set to the standard deviation of these four measurements divided by 2 (the square root of the number of measurements). The VISIR calibration webpage-given flux density for HD 220440 (9.78 Jy) seemed to be too low compared to satellite measurements, so we constructed a broad-band spectral energy distribution for the star from available high-fidelity photometry and fit a stellar atmospheric model to it (e.g., Cotten & Song 2016). From the model fit we estimated the flux in the PAH1 filter bandpass to be 10.37 Jy and used that when flux-calibrating the extracted counts for TYC 8830 410 1. Photometric measurements for TYC 8830 410 1, including from VISIR, are given in Table 3.

Spectroscopic data reduction followed that done for Subaru/COMICS data in Su *et al.* (2020). Slight changes were made to the code to account for different spectrum projections onto the VISIR detector and the presence of two negative spectral beams in the VISIR data; only spectral samples with signal-to-noise ratio per pixel of $\gtrsim 3$ were kept for the final spectrum. From the final combined mid-infrared spectral data set we measure a signal-to-noise ratio of ≈ 10 near $10.5\,\mu m$

3.4. *WISE*

Wide-field Infrared Survey Explorer (*WISE*, Wright *et al.* 2010; Mainzer *et al.* 2011; Mainzer *et al.* 2014) epoch data products are used to explore variability in the TYC 8830 410 1 system in the thermal- to mid-infrared (W1/3.35 μm, W2/4.60 μm, W3/11.56 μm, and W4/22.09 μm channels). The W3 and W4 channels only collected data over a short time period between MJD 55,324-55,326. Data were accessed via IRSA[1] and are taken as reported.

3.5. **ASAS-SN**

All-Sky Automated Survey for Supernovae (ASAS-SN) photometry data products (e.g., Shappee *et al.* 2014; Jayasinghe *et al.* 2019) were utilized in assessing the history of dimming events toward TYC 8830 410 1. We additionally downloaded data products for stars nearby in the plane of the sky to TYC 8830 410 1 with comparable magnitudes for comparison purposes.

3.6. *TESS*

Transiting Exoplanet Survey Satellite (*TESS*; Ricker *et al.* 2014) data are available for TYC 8830 410 1 in two sectors. Full-frame image (FFI) data were obtained during observations of Sector 1 while 2 minute cadence data were obtained during Sector 28. A lightcurve from the FFI data products is obtained from the reductions performed by Huang *et al.* (2020a,b). We additionally reject some data points based on quality flags, unusual character within the time range of BJD 2,458,347-2,458,350, and an additional buffer region on either side of the downlink gap (BJD 2,458,337.8-2,458,340.4). Shorter cadence data are simple aperture photometry (SAP) flux values as retrieved from MAST[2].

3.7. **LCOGT**

Las Cumbres Observatory Global Telescope (LCOGT; Brown *et al.* 2013) monitoring of TYC 8830 410 1 has been ongoing since April 2020. In this paper we present single-band monitoring data obtained through the end of September 2020; multi-band monitoring data has been obtained since then and will be presented in future works.

Images are acquired with the 0.4m robotic telescope network and were requested to be obtained with a cadence of 2 hours. The 0.4m network is a system of Meade 16-inch telescopes equipped with SBIG

---

[1] https://irsa.ipac.caltech.edu/Missions/wise.html

[2] https://mast.stsci.edu/portal/Mashup/Clients/Mast/Portal.html

STL6303 cameras. The cameras host detectors with a plate scale of $0.571''$ pixel^{-1} and a field-of-view of $29'\times19'$. Throughout the 2020 observing period presented herein, only two southern-hemisphere sites were operating − Siding Spring Observatory in Australia and Sutherland Observatory in South Africa. For each visit, telescope guiding was active and three images of 10 seconds each were obtained of TYC 8830 410 1 with the telescope pointing center within $30''$ of the target star. Images were obtained in a Bessel V-band filter.

Data are reduced by LCOGT with the BANZAI data pipeline (McCully *et al.* 2018). In brief, this pipeline corrects for bad pixels, subtracts bias and dark current, performs flat-field correction, conducts source extraction with the SEP software suite[3], and then attempts to obtain an astrometric solution with the methods of http://astrometry.net/. Only images where a successful astrometric solution is obtained are used in subsequent analysis. Due to strongly variable seeing and telescope focus between epochs, we adopt Kron-aperture (Kron 1980) magnitudes as produced by SEP for the target and comparison stars; this choice effectively ensures that the target and comparison stars have apertures with similar encircled energy in every epoch.

A selection of stars within the LCOGT imaging field-of-view with similar brightness as TYC 8830 410 1 are used as comparison stars to derive magnitude measurements for the target star in each epoch. Two comparison stars reproduce well each others' known V-band magnitudes and show no obvious trends throughout the LCOGT monitoring period. These stars have J2000 positions of 23 00 11.84 −58 54 34.6 and 23 00 27.61 −58 57 32.4 and have V-band magnitudes of 12.25 and 12.37, respectively (these are a combination of ASAS-SN and *Gaia* results for both stars and have uncertainty of ∼1%). For each visit, we adopt the median value of the three measured magnitudes for TYC 8830 410 1 as the epoch measurement and the standard deviation as the uncertainty. All measurements are reported in the Appendix in Table A1.

4. RESULTS

4.1. Stellar properties

As the FEROS spectra for TYC 8830 410 1 do not display significant variability (see below), we combine them all into one super-spectrum to characterize the star. From the line ratios of Strassmeier & Fekel (1990) and Padgett (1996) we determine that the star has an effective temperature of 5300 ± 400 K and a spectral type of G9±2, respectively. These are consistent with the results from analysis of RAVE spectra as discussed above, although less precise in general, thus we adopt the RAVE spectroscopic-derived stellar effective temperature and overall spectral type for the star of G9 V (Table 1). In the FEROS super-spectrum we are unable to detect Li I λ6708 absorption and set a 3σ equivalent width limit of <7 mÅ (Figure 1). The bluest orders of the FEROS spectra are then searched for evidence of chromospheric emission in the Ca II H+K lines; no obvious core-reversal emission is seen (Figure 1). Following the methodology of Hempelmann *et al.* (2016) and references therein, we calculate an S-index of 0.26 ± 0.01 from the FEROS super-spectrum and convert it to $\log R'_{HK}$ of -4.75 ± 0.10 following the description in Noyes *et al.* (1984).

Gaia proper motion and parallax measurements for stars in the field around TYC 8830 410 1 reveal a $49.5''$ separation co-moving and co-distant companion. This star, 2MASS J23011901−5858262 (hereafter 2MASS J2301−5858), has an absolute magnitude and $G_{BP}-G_{RP}$ color (Table 1) that strongly suggest it is a mid-M dwarf star. MagE spectra of the companion (Figure 2) demonstrate it is consistent with a spectral type of M4 V, has moderately strong Balmer Hα emission (equivalent width of 2.1 ± 0.1 Å, presumably due to magnetic activity), and has no detectable Li I λ6708 absorption (with a 3σ equivalent width limit of <60 mÅ). We additionally measure a radial velocity for the companion consistent with the average of FEROS velocity measurements for the primary star (Tables 1 and 2),

---

[3] https://github.com/kbarbary/sep

thus further confirming them to be truly bound.

Radial velocity data from FEROS (and to a lesser degree other available radial velocity measurements in Table 2) are used to search for and constrain the presence of other companions to TYC 8830 410 1. Taken at their quoted uncertainties, the FEROS velocities suggest variability is present at the level of $\sim$0.1 km s^{-1}. A periodogram search of the FEROS velocities does not indicate any significant signals are present, but are suggestive of a possible period around $\approx$4 days. Continued radial velocity monitoring of TYC 8830 410 1 can determine if this signal is real and whether it is due to stellar activity, possibly a hot Jupiter-like companion, or maybe due to transiting dust clouds as described in Dodin & Suslina (2021). With no significant signals present in the FEROS velocity data, we conclude that there are no stellar-mass nor massive sub-stellar companions within an AU of TYC 8830 410 1.

4.2. **Infrared excess emission**

We revisit the infrared excess parameters presented in Cotten & Song (2016) based on updated stellar and infrared measurements presented herein. Figure 3 shows that this system hosts warm inner planetary system dust with strong solid-state emission resulting in a fractional infrared luminosity of $\sim$1%, easily placing it in league with other exceptionally dusty main sequence star systems (e.g., Melis 2016; Moór *et al.* 2021). High spatial resolution VLT/VISIR mid-infrared imaging observations find only a single point source, indicating that this object is the source of the *WISE*-detected excess flux, thus confirming it as a bona-fide exceptionally dusty inner planetary disk system.

Stellar parameters retrieved from the spectral energy distribution fit suggest an effective temperature of $\approx$5,000 K which is lower (albeit not especially significantly) than the spectroscopically-retrieved value of 5,350 K. As discussed below, the star is likely to be seen through a varying level of dust and thus could be reddened leading to the lower spectral energy distribution fit-value. We attempted a second stellar spectral energy distribution fit with the model effective temperature fixed at 5,300 K and found a reddening of A_V=0.5 mag with the Cardelli *et al.* (1989) extinction curve (and R_V=3.1) provides a reasonable fit to the stellar photometry. Additional evidence for reddening appears in the color-magnitude diagram position of TYC 8830 410 1 as discussed in Section 5.1.

The VISIR mid-infrared spectrum (Figures 3 and 4) clearly reveals a strong solid-state emission feature with the characteristic amorphous and crystalline silicate peaks at $\approx$10 and 11 μm (e.g., Honda *et al.* 2004, Chen *et al.* 2006, Lisse *et al.* 2008). Fitting proceeds as in Weinberger *et al.* (2011) and Olofsson *et al.* (2012), which we briefly summarize here. We used the same optical constants and absorption coefficients as in Olofsson *et al.* (2012); these are taken from Dorschner *et al.* (1995) and Jäger *et al.* (2003) for amorphous silicates with olivine and pyroxene stoichiometry, from Tamanai & Mutschke (2010) for the "Mg-rich" and "Fe-rich" crystalline olivine, from Tamanai (2010) for the silica, from Jäger *et al.* (1998a) for the crystalline enstatite, and from Jäger *et al.* (1998b) for the carbonaceous dust grains. For all the dust species, the minimum allowed grain size is 0.1 μm while the maximum grain size is set to 1 μm for the crystalline dust grains and 1 mm for the amorphous dust species. The free parameters of the modeling are the inner radius and radial width of the dust ring, the slope of the density distribution, and the slope of the grain size distribution. The radial distribution is sampled over $n_r = 80$ bins, and for each dust species and each grain size the temperature of the particles at a given distance is calculated by equating the energy received and emitted (Eqn. 3 of Olofsson *et al.* 2012). For each dust species, we then compute an emission profile at the same wavelengths as the observations, weighted by the grain size distribution. For a given set of free parameters, we then find the linear combination of the emission profiles that best reproduces the observed spectrum, using the `lmfit` package (Newville *et al.* 2021). To find the best solution, we used the `Multinest` nested sampling algorithm (Feroz *et al.* 2009, 2019), interfaced with `Python` using the `PyMultiNest` package (Buchner *et al.* 2014).

From the available spectrum we are able to constrain the inner radius of the disk of emitting dust grains to be ∼0.25 AU (and certainly <0.5 AU) and the crystallinity fraction to being ∼30% by mass. We are not able to robustly constrain the type of emitting grains (although some combination of forsterite and enstatite most likely contribute to the 11 μm shoulder) and that the grain size distribution favors small (<2 μm) dust particles. A representative fit illustrating these dust properties is shown in Figure 4.

It is found that the dust continuum temperature is not well-constrained as most available excess measurements are part of the solid state emission complex (we assume there are strong silicate emission features near ∼20 μm that enhance the *WISE W*4 measurement). In arriving at the continuum curves plotted in Figure 3, we require the fit to pass through the bottom of the high- and low-wavelength ends of the VISIR N-band spectrum. In doing so, we arrive at temperatures T_{dust} of 300-350 K.

4.3. **Occultations**

TYC 8830 410 1 was observed with *TESS* in Sector 1 as a Full-Frame Image target (30 minute cadence). The beginning of the *TESS* lightcurve just catches a ∼1 magnitude deep, ≈1.5 day duration eclipse with irregular shape (Figure 5). Also evident is general variability with a stochastic nature to it (no identifiable period within the ≈28-day timespan). Examining precovery ASAS-SN lightcurve data for TYC 8830 410 1 shows several dips compatible with the depth of the *TESS*-observed feature as well as stochastic variability that results in a lightcurve rms deviation from the mean of ≈0.14 magnitudes (Figure 6). A periodogram for the ASAS-SN data does not reveal significant signals at any period. Phase-folding the lightcurve across a range of values reveals that some periods between 120-200 days can line up most of the dips, but not all of them.

ASAS-SN lightcurve data for stars nearby and of comparable brightness to TYC 8830 410 1 do not show any dips nor the stochastic variability (ASAS-SN check stars showed rms fluctuations in their lightcurves at the 0.01-0.02 magnitude level). We also examined *TESS* data for similar magnitude stars around TYC 8830 410 1 and did not find any others with comparable features. This leads us to conclude that the features observed in the optical data are astrophysical and not instrumental in nature. *WISE* epoch photometry spanning precovery to post-*TESS* Sector 1 epochs are suggestive of possible deep eclipses even in the thermal infrared. However, after comparison with nearby stars of similar magnitude as TYC 8830 410 1, it is determined that apparent dips are actually instrumental in nature.

Based on the *TESS* eclipse feature and support for occultations from ASAS-SN, we pursued additional *TESS* data in the extended mission with a higher cadence and ground-based routine monitoring with LCOGT. LCOGT monitoring shows a wide range of variability, including ∼1 day duration deep eclipses and a host of smaller depth features of various durations (Figure 6). The LCOGT data display an rms deviation from the mean of ≈0.17 magnitudes, reasonably consistent with that seen in the ASAS-SN data (meaning no obvious evolution of the dust screen has occurred in the ∼6.5 years of observations presented herein). The 2 minute cadence lightcurve from *TESS* Sector 28 overlaps with LCOGT monitoring and similarly shows highly structured variability (Figures 5). In general the appearance of *TESS* and LCOGT/ASAS-SN data where they overlap are similar, although there are some disagreements (especially in the absolute flux level) that could be instrumental or possibly astronomical in nature (*TESS* has a redder bandpass than the V-band monitoring done with LCOGT and ASAS-SN). Ongoing and future ground-based multiband observations can reveal if the depth of eclipse features are wavelength dependent.

We group the types of dimming events for TYC 8830 410 1 into three categories. In the first category is the stochastic variability when the star is between V-band magnitudes of 11.4 to 12.1. The brightest V-band magnitude measured with ASAS-SN or LCOGT for TYC 8830 410 1 is 11.46±0.01, which we

take to be the unocculted V-band magnitude. In the second category are medium dimming events where the star fades to V-band magnitudes of 12.2 to 12.3. The third category is for the deep dimming events when the star is extinguished to V-band magnitudes of fainter than 12.3. Each of ASAS-SN, *TESS* (in the two different sectors), and LCOGT see all three categories in their monitoring data.

5. DISCUSSION

5.1. System age

Estimates for the age of the TYC 8830 410 1 system must be self-consistent for both stars. In addition to measurements described above, we also include an X-ray upper limit from *ROSAT* (Truemper 1982) and *eROSITA* (extended ROentgen Survey with an Imaging Telescope Array; Predehl *et al.* 2021) for TYC 8830 410 1 (and technically its companion, although that is less constraining), 3D Galactic space kinematics (Table 1), and simultaneous isochrone fits for both stars.

Lithium limits for TYC 8830 410 1 rule out ages ≤ 100 Myr and suggest an age $\gtrsim 200$ Myr (e.g., Zuckerman & Song 2004). The non-detection of lithium in the companion spectrum is consistent with these age bounds, although in and of itself is not especially constraining (suggesting ages $\gtrsim 20$ Myr).

Analysis of RAVE Ca II infrared triplet data suggested an age of ≈ 370 Myr (Žerjal *et al.* 2017). Our analysis of Ca II H+K activity levels from the FEROS data suggest an age range of 1.5-4.0 Gyr if one applies directly Equation 3 of Mamajek & Hillenbrand (2008). However, if one instead considers Figures 4 and 5 and Tables 7 and 9 of Mamajek & Hillenbrand (2008) it is possible $-$ given the range of $\log R'_{HK}$ values observed for various open cluster members of known age $-$ that TYC 8830 410 1 could be between 100 Myr and 4 Gyr. The extremes of the latter age range would require TYC 8830 410 1 to be an activity outlier while ages between 600 Myr to 2 Gyr are more likely to produce the observed activity level. As such, we consider chromospheric activity to rule out ages < 100 Myr and to be suggestive of an age $\gtrsim 500$ Myr. Chromospheric activity for the companion star in the form of Hα emission is consistent with chromospheric ages suggested for the primary star, and specifically suggests an age $\lesssim 2$ Gyr (e.g., Shkolnik *et al.* 2009; Kiman *et al.* 2021, and references therein).

The *ROSAT* all-sky survey and first *eROSITA* all-sky survey did not detect TYC 8830 410 1 nor its companion in the X-rays (A. Merloni 2021, priv. comm.). *eROSITA* provides better sensitivity than does *ROSAT*, so we focus discussion on its X-ray limits. We obtain X-ray limits by assessing the flux and associated uncertainties for detected sources in the region of TYC 8830 410 1. A conservative limit of the $\approx 95\%$ source completeness level is adopted, resulting in a flux limit in the 0.6-2.3 keV band of $< 2 \times 10^{-13}$ ergs cm^{-2} s^{-1}. The *eROSITA* limit suggests a ratio of X-ray to bolometric luminosity for TYC 8830 410 1 of $\log(L_X/L_{bol}) < -3.6$ and a limit for its companion of $\log(L_X/L_{bol}) < -2.0$. Comparison to Figure 4 of Zuckerman & Song (2004) suggests the primary is $\gtrsim 100$ Myr old. Limits for the companion are not especially restrictive (e.g., Zuckerman & Song 2004; Stelzer *et al.* 2013).

Three-dimensional Galactic space motions (UVW in Table 1) are compatible with young stars ($\lesssim 100$ Myr) within 200 pc of the Sun (e.g., Zuckerman & Song 2004; Torres *et al.* 2008). Interestingly, the best matches between the UVW space motions for the TYC 8830 410 1 system and known nearby moving groups are ϵ Cha and the Local Association or Pleiades moving group. The former is far too young to be home to TYC 8830 410 1 (with an age of ~ 6 Myr), in addition to inconsistencies between their respective distances and locations on the plane of the sky (Torres *et al.* 2008). The legitimacy of the latter association is questionable (e.g., Zuckerman & Song 2004) and in any case is suggested to mostly have ages between 20-150 Myr (Montes *et al.* 2001 and references therein), again incompatible with age constraints for TYC 8830 410 1 discussed above. Other possible matches also suffer distance, age, or positional issues (e.g., Gagné *et al.* 2018b; Baluev *et al.* 2020). TYC 8830 410 1 appears to have a young-star-like UVW space motion by coincidence, but otherwise is not particularly young (as suggested by other age indicators). In such a case, kinematics are not capable of placing any reasonable constraints on the age of the system.

Attempts to age-date the TYC 8830 410 1 system via simultaneous isochrone fitting are confounded by what appears to be reddening of the primary star. In most color-absolute magnitude diagrams TYC 8830 410 1 appears either too bright or too red (e.g., Figure 7). Based on the evidence for significant (and variable) quantities of dust lying along our line of sight to the primary star, we consider it to be reddened. We do, however, mention briefly and dismiss the possibility that TYC 8830 410 1 itself could be an unresolved binary system composed of nearly equal-mass stars. This setup is highly contrived as it would require the binary orbit to not exhibit obvious radial velocity variability (a nearly face-on orbital inclination or wide orbit; see restrictions in Section 4.1) and to have orbital parameters that allow the inner disk component to exist over decade timescales (see Section 4.3).

Given the issues with the primary discussed above, we rely on the position of the companion alone to inform isochrone age estimates. In all colors explored (Figure 7), 2MASS J2301−5858 lies above the locus of field stars of similar spectral type and tends to agree well with colors and absolute magnitudes of mid-M-type Hyades stars. As such, we adopt isochrone age bounds of >500 Myr and <5 Gyr.

Taking in aggregate all of the above age bounds, we can confidently rule out ages <200 Myr for the TYC 8830 410 1 system. The best age estimate is roughly Hyades-aged ($\approx$600 Myr), but the system could very well be between 500 Myr-2 Gyr in age. X-ray detections of both stars could help improve the age estimate for this system, as well as high signal-to-noise ratio optical spectroscopy monitoring the Ca II H+K chromospheric activity (especially if a stellar rotation period could be measured).

Based on the best age estimate above, TYC 8830 410 1 is intermediate in age relative to other known extremely dusty main sequence stars which span from several Myr to >1 Gyr (e.g., Melis 2016; Moór *et al.* 2021, and references therein). Notably, most extreme debris disk systems have ages $\lesssim$200 Myr with the exceptions of BD+20 307 (age >1 Gyr, Zuckerman *et al.* 2008; Moór *et al.* 2021) and TYC 4479 3 1 (age 5±2 Gyr, Moór *et al.* 2021). The latter system we consider to be contaminated by Galactic dust emission (see Figure 1 of Moór *et al.* 2021 where extended nebular emission overlapping with the star is clearly evident in the *WISE* channels where excess is claimed); it needs to be confirmed with higher resolution mid-infrared imaging before being included in any extremely dusty main sequence star analyses. As such, TYC 8830 410 1 and BD+20 307 are the oldest (confirmed) extremely dusty main sequence stars known and TYC 8830 410 1 the oldest such system where the dusty debris eclipses the host star (robust ages are not yet known for systems presented by Tajiri *et al.* 2020).

TYC 8830 410 1 joins the growing number of extremely dusty main sequence stars with wide-separation binary companions. This association was first noted by Zuckerman (2015) and expanded upon in Moór *et al.* (2021). The assertion by Moór *et al.* (2021) that such dusty systems are more likely to host wide separation companions as a function of age is supported by the age estimate for TYC 8830 410 1 derived here. Moór *et al.* (2021) develop a cometary delivery model to explain the origin of extremely dusty main sequence stars − especially the older population − and suggest perhaps such delivery is amplified by instabilities due to wide separation companions. The cometary model proposed by Moór *et al.* (2021) suffers from a major weakness in that any instability which sends a significant quantity of mass to a star's inner planetary system should also produce a substantial population of small dust grains in the star's outer planetary system (e.g., Fujiwara *et al.* 2012b; Bonsor *et al.* 2013, 2014; Raymond & Bonsor 2014, and references therein). Indeed, Moór *et al.* (2021) acknowledge this shortcoming of their proposed cometary model and note results by Vican *et al.* (2016) which show very few extremely dusty main sequence stars host outer planetary system dust populations consistent with a cometary model. In Section 6 we suggest an alternative model that will be explored further in later works.

5.2. **Dust properties**

With a fractional infrared luminosity of ∼1%, TYC 8830 410 1 is not especially remarkable amongst the currently known sample of extremely dusty main sequence stars. The dust composition is at first glance reasonably compatible with what is seen for other such stars (e.g., Olofsson *et al.* 2012 and references therein), although the available data leaves ambiguous many of the dust properties. One potentially interesting difference that remains to be conclusively measured is an apparent enstatite dominance over forsterite. In some of our models there can be as much as a factor of 2 more enstatite than forsterite which is not typically seen in extremely dusty star disks (e.g., Fujiwara *et al.* 2010; Olofsson *et al.* 2012). Enstatite-rich bodies are known in the solar system, including the surface of Mercury and E-type asteroids which make up a significant fraction of the inner asteroid belt (e.g., Sprague & Roush 1998; Zellner *et al.* 1977; Keil *et al.* 1989). Future comprehensive mid-infrared spectroscopy (e.g., with *JWST*) can help establish if this result is robust for TYC 8830 410 1.

With the photometric monitoring conducted to date it is not possible to demonstrate if the deeper dips seen are (quasi-)periodic or aperiodic. Routine monitoring at a cadence of ≲1 day without gaps in temporal coverage is essential to catch these events or conclusively say they did not occur. For example, the sporadic cadence of the ASAS-SN monitoring could easily have missed any number of ∼1.5 day duration events like those seen in the *TESS* and LCOGT data. Two such events are found in the LCOGT monitoring from April to September 2020 separated by about 82 days, although the April event was captured with a single epoch only and sufficient gaps in coverage are present that other events could have been missed. Even allowing for missed events, it is not possible to find a periodic spacing that matches the four lowest measured magnitudes in the ASAS-SN data, the deep dip in the *TESS* data, and the two deep dips in the LCOGT data. A period near 180 days can get close to lining up most of the ASAS-SN and first LCOGT deep dips, but not the *TESS* and second LCOGT deep dips which appear to themselves be separated by a factor of roughly 180 days. A speculative idea is that we might be seeing multiple orbiting sites of major collisions that shear out and disperse with time.

Stochastic variability similarly has no discernible period associated with it. This combined with a lack of strong magnetic activity on TYC 8830 410 1 indicates that this variability must also be due to dust transiting across the face of the star. The medium dimming events are a few times more frequent than deep dimming events and tend to be longer in duration (∼3 days in the *TESS* Sector 28 lightcruve), but again show no clear periodicity in the available data.

We conclude that all variability seen in optical lightcurves for TYC 8830 410 1 is due to transiting dust. It is not possible to robustly identify the configuration of such dust with the available data, but we comment on two possibilities. In one configuration, the dust disk is vertically thin (scale height ≲ the stellar diameter), radially narrow ($\Delta R_{dust} < 0.1\,R_{dust}$), and the dust is fairly homogeneous in density in the vertical and radial axes. In this case all the lightcurve changes are due to changes in the azimuthal density in the dust and indicate substantial clumpiness in the dust ring. Such a configuration would be reminiscent of the distribution of material presented in Watt *et al.* (2021) for post-giant impact-type events. Adapting the models of Watt *et al.* (2021) to predict stellar brightness changes if post-collision dusty ejecta transits the host star would be valuable in further assessing the nature of TYC 8830 410 1 and possibly the systems presented by Gaidos *et al.* (2019) and Tajiri *et al.* (2020).

In a another − perhaps more contrived − configuration, the dust disk is again radially narrow and the density is homogeneous in the radial and azimuthal axes. The disk has a structured vertical density distribution and is additionally warped and precessing. Such a configuration has been suggested for pre-main sequence "dipper" stars where gas and/or interactions with stellar magnetic fields help shape the disk inner edge (e.g., Bouvier *et al.* 2003 and references therein). However, there is currently no evidence for gas in the disk around TYC 8830 410 1, and it appears to lie at orbital

separations well beyond the reaches of the stellar magnetic field (Section 4.2). As such, any vertical structuring in its disk (if present) would have to come from other sources, perhaps from Kozai-Lidov-type interactions with the wide M-type companion. In this case the changes in the lightcurve are due to the different heights in the disk being probed by the line of sight to the star. They would not be strictly periodic due to the precession of the warp and possibly due to warp evolution.

6. **CONCLUSIONS**

We present detailed characterization of the TYC 8830 410 1 system. Infrared excess emission from circumstellar dust is seen and occultations from this dust are caught in stellar photometric monitoring. TYC 8830 410 1 appears to have an age of ∼600 Myr, and is definitely older than typical extremely dusty main sequence stars which have ages of ≲200 Myr.

The unusual deep dimming event shape, lack of a companion detection in radial velocity measurements, the general stochastic variability seen in lightcurves, and the strong mid-infrared excess emission with clear solid-state emission from small dust grains point to a possible origin of the transit events as due to dust released in the aftermath of a giant impact between rocky planets. Giant impact-type collisions would produce significant quantities of dusty ejecta that would go into orbit around the host star (e.g., Melis *et al.* 2010; Jackson & Wyatt 2012; Genda *et al.* 2012; Watt *et al.* 2021, and references therein). Ejecta would collisionally grind itself down generating small dust grains that would produce the observed mid-infrared excess emission and the stochastic variability (similar to what is seen in Gaidos *et al.* 2019). Clumps of dust, or dust around the post-impact rocky planet (possibly in a proto-lunar disk configuration; e.g., Kokubo *et al.* 2000) could be responsible for the deep dips seen if they subtend a large angular size relative to the host star they orbit (e.g., Mamajek *et al.* 2012; Kenworthy & Mamajek 2015).

The implied giant impact-type event is unlikely to be associated with rocky planet formation given the intermediate age of TYC 8830 410 1 (such events should occur for stellar ages ≲100 Myr; e.g., Hartmann & Davis 1975; Genda *et al.* 2015; Levison *et al.* 2015) and instead could possibly be due to a late-stage instability (e.g., Izidoro *et al.* 2019; Moór *et al.* 2021 and references therein). Izidoro *et al.* (2019) specifically follow the long-term dynamical evolution of planetary systems that form as chains of first order mean motion resonances (resonant chains), finding that up to ≈95% of resonant chains become dynamically unstable after dispersal of the gas disk. They find timescales for these instabilities that extend up to the limit of their simulations (≈300 Myr), and it could be the case that such instabilities could occur for even older ages. Eccentricities and orbital inclinations of planets in a resonant chain grow in the absence of the damping effects of the gas disk due to mutual interactions and their orbits can eventually cross leading to collisions and scattering events. Eccentricities and relative velocities could be further enhanced by the effects of a widely separated companion (like 2MASS J2301−5858 in the case of the TYC 8830 410 1 system) through the Kozai-Lidov mechanism (e.g., Nesvold *et al.* 2016 and references therein) increasing the likelihood of instability and destructive collisions. This instability-driven phase of late giant impacts would be where the dust seen in extremely dusty stars like TYC 8830 410 1 originates from.

If the proposed interpretation for TYC 8830 410 1 is correct, then it would serve as a Rosetta stone for understanding exceptionally dusty stars. It would be capable of providing the first-ever detailed look at the structure of post-giant impact ejecta and its evolution, thus allowing direct tests and constraints on models of this important pathway for rocky planet evolution. Multi-band monitoring of this system is essential in conducting such work, and with a reasonable brightness of $V_{mag} \sim 12$ amateurs could easily contribute.

REFERENCES

Ansdell, M., *et al.* 2019, *MNRAS*, **483**, 3579

Balog, Z., *et al.* 2009, *ApJ*, **698**, 1989

Baluev, R. V., Shaidulin, V. S., & Veselova, A. V. 2020, *AcA*, **70**, 141

Bonsor, A., Raymond, S. N., & Augereau, J.-C. 2013, *MNRAS*, **433**, 2938

Bonsor, A., Raymond, S. N., Augereau, J.-C., & Ormel, C. W. 2014, *MNRAS*, **441**, 2380

Bouvier, J., *et al.* 2003, *A&A*, **409**, 169

Boyajian, T. S., *et al.* 2016, *MNRAS*, **457**, 3988

— 2018, *ApJL*, **853**, L8

Brahm, R., Jordán, A., & Espinoza, N. 2017, *PASP*, **129**, 034002

Brown, T. M., *et al.* 2013, *PASP*, **125**, 1031

Buchner, J., *et al.* 2014, *A&A*, **564**, A125

Cardelli, J. A., Clayton, G. C., & Mathis, J. S. 1989, *ApJ*, **345**, 245

Chen, C. H., *et al.* 2006, *ApJS*, **166**, 351

Cody, A. M., *et al.* 2014, *AJ*, **147**, 82

Cohen, M., Walker, R. G., Carter, B., Hammersley, P., Kidger, M., & Noguchi, K. 1999, *AJ*, **117**, 1864

Cotten, T. H. & Song, I. 2016, *ApJS*, **225**, 15

Cutri, R. M., *et al.* 2003, *2MASS All Sky Catalog of point sources.*, The IRSA 2MASS All-Sky Point Source Catalog, NASA/IPAC Infrared Science Archive. http://irsa.ipac.caltech.edu/applications/Gator/

Cutri, R. M. e. 2012, *VizieR Online Data Catalog*, **2311**, 0

David, T. J., *et al.* 2017, *ApJ*, **835**, 168

de Wit, W. J., Grinin, V. P., Potravnov, I. S., Shakhovskoi, D. N., Müller, A., & Moerchen, M. 2013, *A&A*, **553**, L1

Dodin, A. V. & Suslina, E. A. 2021, *arXiv e-prints*, arXiv:2102.08911

Dorschner, J., Begemann, B., Henning, T., Jaeger, C., & Mutschke, H. 1995, *A&A*, **300**, 503

Epchtein, N., *et al.* 1999, *A&A*, **349**, 236

Feroz, F., Hobson, M. P., & Bridges, M. 2009, *MNRAS*, **398**, 1601

Feroz, F., Hobson, M. P., Cameron, E., & Pettitt, A. N. 2019, *The Open Journal of Astrophysics*, **2**, 10

Fouqué, P., *et al.* 2000, *A&AS*, **141**, 313

Fujiwara, H., *et al.* 2010, *ApJL*, **714**, L152

— 2012a, *ApJL*, **749**, L29

— 2012b, *ApJL*, **759**, L18

Gagné, J., Faherty, J. K., & Mamajek, E. E. 2018a, *ApJ*, **865**, 136

Gagné, J., *et al.* 2018b, *ApJ*, **856**, 23

Gaia Collaboration, Brown, A. G. A., Vallenari, A., Prusti, T., de Bruijne, J. H. J., Babusiaux, C., & Biermann, M. 2020, *arXiv e-prints*, arXiv:2012.01533

Gaia Collaboration, *et al.* 2018, *A&A*, **616**, A1

Gaidos, E., *et al.* 2019, *MNRAS*, **488**, 4465

Genda, H., Kobayashi, H., & Kokubo, E. 2015, *ApJ*, **810**, 136

Genda, H., Kokubo, E., & Ida, S. 2012, *ApJ*, **744**, 137

Gorlova, N., Balog, Z., Rieke, G. H., Muzerolle, J., Su, K. Y. L., Ivanov, V. D., & Young, E. T. 2007, *ApJ*, **670**, 516

Gorlova, N., *et al.* 2004, *ApJS*, **154**, 448

Gossage, S., Conroy, C., Dotter, A., Choi, J., Rosenfield, P., Cargile, P., & Dolphin, A. 2018, *ApJ*, **863**, 67

Hartmann, W. K. & Davis, D. R. 1975, *Icarus*, **24**, 504

Hauschildt, P. H., Allard, F., & Baron, E. 1999, *ApJ*, **512**, 377

Hempelmann, A., Mittag, M., Gonzalez-Perez, J. N., Schmitt, J. H. M. M., Schröder, K. P., & Rauw, G. 2016, *A&A*, **586**, A14

Henden, A. A., Levine, S., Terrell, D., & Welch, D. L. 2015, in *American Astronomical Society Meeting Abstracts #225*, vol. 225 of *American Astronomical Society Meeting Abstracts*, 336.16

Honda, M., *et al.* 2004, *ApJL*, **610**, L49

Huang, C. X., *et al.* 2020a, *Research Notes of the American Astronomical Society*, **4**, 204

— 2020b, *Research Notes of the American Astronomical Society*, **4**, 206

Izidoro, A., Bitsch, B., Raymond, S. N., Johansen, A., Morbidelli, A., Lambrechts, M., & Jacobson, S. A. 2019, *arXiv e-prints*, arXiv:1902.08772

Jackson, A. P. & Wyatt, M. C. 2012, *MNRAS*, **425**, 657

Jäger, C., Dorschner, J., Mutschke, H., Posch, T., & Henning, T. 2003, *A&A*, **408**, 193

Jäger, C., Molster, F. J., Dorschner, J., Henning, T., Mutschke, H., & Waters, L. B. F. M. 1998a, *A&A*, **339**, 904

Jäger, C., Mutschke, H., & Henning, T. 1998b, *A&A*, **332**, 291

Jayasinghe, T., *et al.* 2019, *MNRAS*, **485**, 961

Johnson, D. R. H. & Soderblom, D. R. 1987, *AJ*, **93**, 864

Kaufer, A., *et al.* 1999, *The Messenger*, **95**, 8

Käufl, H. U., *et al.* 2015, *The Messenger*, **159**, 15

Keil, K., Ntaflos, T., Taylor, G. J., Brearley, A. J., Newsom, H. E., & Romig, A. D. J. 1989, *GeoCoA*, **53**, 3291

Kelson, D. D. 2003, *PASP*, **115**, 688

Kelson, D. D., Illingworth, G. D., van Dokkum, P. G., & Franx, M. 2000, *ApJ*, **531**, 159

Kennedy, G. M., Kenworthy, M. A., Pepper, J., Rodriguez, J. E., Siverd, R. J., Stassun, K. G., & Wyatt, M. C. 2017, *Royal Society Open Science*, **4**, 160652

Kennedy, G. M. & Wyatt, M. C. 2013, *MNRAS*, **433**, 2334

Kenworthy, M. A. & Mamajek, E. E. 2015, *ApJ*, **800**, 126

Kiman, R., *et al.* 2021, *arXiv e-prints*, arXiv:2104.01232

Kokubo, E., Ida, S., & Makino, J. 2000, *Icarus*, **148**, 419

Kral, Q., *et al.* 2017, *The Astronomical Review*, **13**, 69

Kron, R. G. 1980, *ApJS*, **43**, 305

Kunder, A., et al. 2017, AJ, **153**, 75

Lagage, P. O., et al. 2004, The Messenger, **117**, 12

Levison, H. F., Kretke, K. A., Walsh, K. J., & Bottke, W. F. 2015, Proceedings of the National Academy of Science, **112**, 14180

Lisse, C. M., Chen, C. H., Wyatt, M. C., & Morlok, A. 2008, ApJ, **673**, 1106

Mainzer, A., et al. 2011, ApJ, **731**, 53

— 2014, ApJ, **792**, 30

Mamajek, E. E. & Hillenbrand, L. A. 2008, ApJ, **687**, 1264

Mamajek, E. E., et al. 2012, AJ, **143**, 72

Marton, G., Tóth, L. V., Paladini, R., Kun, M., Zahorecz, S., McGehee, P., & Kiss, C. 2016, MNRAS, **458**, 3479

McCully, C., et al. 2018, in Software and Cyberinfrastructure for Astronomy V, edited by J. C. Guzman & J. Ibsen, vol. 10707 of Society of Photo-Optical Instrumentation Engineers (SPIE) Conference Series, 107070K

McDonald, I., Zijlstra, A. A., & Watson, R. A. 2017, MNRAS, **471**, 770

Melis, C. 2016, in Young Stars & Planets Near the Sun, edited by J. H. Kastner, B. Stelzer, & S. A. Metchev, vol. 314, 241–246

Melis, C., Zuckerman, B., Rhee, J. H., & Song, I. 2010, ApJL, **717**, L57

Melis, C., Zuckerman, B., Rhee, J. H., Song, I., Murphy, S. J., & Bessell, M. S. 2012, Nature, **487**, 74

— 2013, ApJ, **778**, 12

Meng, H. Y. A., et al. 2017, ApJ, **847**, 131

Mentel, R. T., et al. 2018, A&A, **619**, A157

Montes, D., López-Santiago, J., Gálvez, M. C., Fernández-Figueroa, M. J., De Castro, E., & Cornide, M. 2001, MNRAS, **328**, 45

Moór, A., et al. 2021, arXiv e-prints, arXiv:2103.00568

Morales-Calderón, M., et al. 2011, ApJ, **733**, 50

Nesvold, E. R., Naoz, S., Vican, L., & Farr, W. M. 2016, ApJ, **826**, 19

Newville, M., et al. 2021, lmfit/lmfit-py 1.0.2

Noyes, R. W., Hartmann, L. W., Baliunas, S. L., Duncan, D. K., & Vaughan, A. H. 1984, ApJ, **279**, 763

Olofsson, J., Juhász, A., Henning, T., Mutschke, H., Tamanai, A., Moór, A., & Ábrahám, P. 2012, A&A, **542**, A90

Padgett, D. L. 1996, ApJ, **471**, 847

Predehl, P., et al. 2021, A&A, **647**, A1

Punzi, K. M., Kastner, J. H., Melis, C., Zuckerman, B., Pilachowski, C., Gingerich, L., & Knapp, T. 2018, AJ, **155**, 33

Rappaport, S., et al. 2019, MNRAS, **485**, 2681

Raymond, S. N. & Bonsor, A. 2014, MNRAS, **442**, L18

Rhee, J. H., Song, I., & Zuckerman, B. 2007, ApJ, **671**, 616

— 2008, ApJ, **675**, 777

Ricker, G. R., et al. 2014, in Space Telescopes and Instrumentation 2014: Optical, Infrared, and Millimeter Wave, edited by J. Oschmann, Jacobus M., M. Clampin, G. G. Fazio, & H. A. MacEwen, vol. 9143 of Society of Photo-Optical Instrumentation Engineers (SPIE) Conference Series, 914320

Saito, R. K., et al. 2019, MNRAS, **482**, 5000

Schneider, A., Song, I., Melis, C., Zuckerman, B., Bessell, M., Hufford, T., & Hinkley, S. 2013, ArXiv e-prints

Shappee, B. J., et al. 2014, ApJ, **788**, 48

Shkolnik, E., Liu, M. C., & Reid, I. N. 2009, ApJ, **699**, 649

Skrutskie, M. F., et al. 2006, AJ, **131**, 1163

Song, I., Zuckerman, B., Weinberger, A. J., & Becklin, E. E. 2005, Nature, **436**, 363

Sprague, A. L. & Roush, T. L. 1998, Icarus, **133**, 174

Stelzer, B., Marino, A., Micela, G., López-Santiago, J., & Liefke, C. 2013, MNRAS, **431**, 2063

Strassmeier, K. G. & Fekel, F. C. 1990, A&A, **230**, 389

Su, K. Y. L., Rieke, G. H., Melis, C., Jackson, A. P., Smith, P. S., Meng, H. Y. A., & Gáspár, A. 2020, ApJ, **898**, 21

Tajiri, T., et al. 2020, ApJS, **251**, 18

Tamanai, A. 2010, in "Dust in Planetary Systems, Workshop, Jena, Germany"

Tamanai, A. & Mutschke, H. 2010, Infrared spectroscopy of dust particles in aerosols for astronomical application, Fundamentals and Applications in Aerosol Spectroscopy, eds. J. Reid and R. Signorell, pp.101-123 (Taylor & Francis Group: Florida)

Torres, C. A. O., Quast, G. R., Melo, C. H. F., & Sterzik, M. F., Young Nearby Loose Associations, 757–+

Truemper, J. 1982, Advances in Space Research, **2**, 241

Uzpen, B., Kobulnicky, H. A., & Kinemuchi, K. 2009, AJ, **137**, 3329

van Werkhoven, T. I. M., Kenworthy, M. A., & Mamajek, E. E. 2014, MNRAS, **441**, 2845

Vican, L., Schneider, A., Bryden, G., Melis, C., Zuckerman, B., Rhee, J., & Song, I. 2016, ApJ, **833**, 263

Žerjal, M., et al. 2017, ApJ, **835**, 61

Watt, L., Leinhardt, Z., & Su, K. Y. L. 2021, MNRAS, **502**, 2984

Weinberger, A. J., Becklin, E. E., Song, I., & Zuckerman, B. 2011, ApJ, **726**, 72

Wright, E. L., et al. 2010, AJ, **140**, 1868

Wyatt, M. C. 2008, ARA&A, **46**, 339

Zellner, B., Leake, M., Morrison, D., & Williams, J. G. 1977, GeoCoA, **41**, 1759

Zuckerman, B. 2015, ApJ, **798**, 86

Zuckerman, B., Fekel, F. C., Williamson, M. H., Henry, G. W., & Muno, M. P. 2008, ApJ, **688**, 1345

Zuckerman, B., Melis, C., Rhee, J. H., Schneider, A., & Song, I. 2012, ApJ, **752**, 58

Zuckerman, B. & Song, I. 2004, ARA&A, **42**, 685
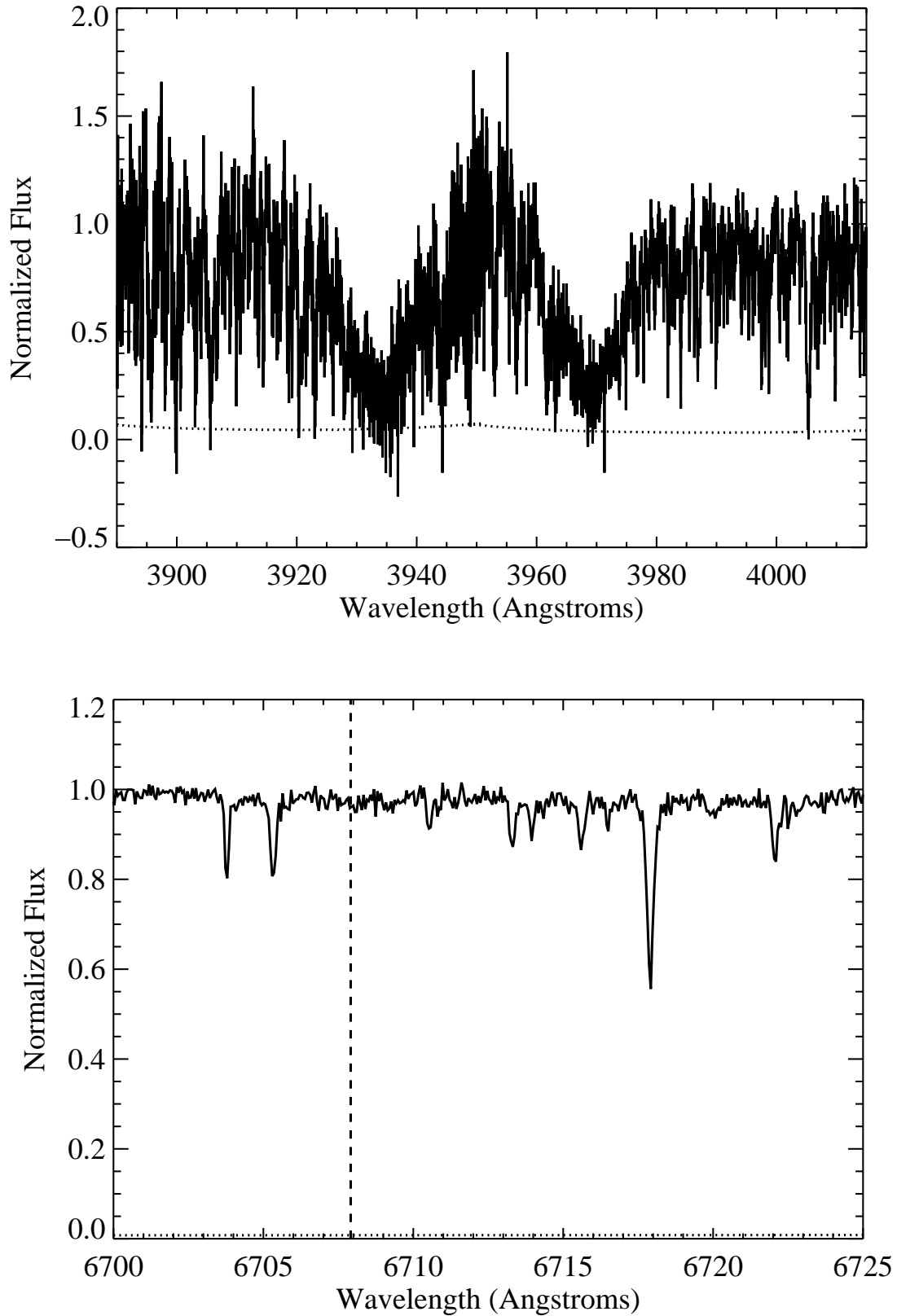
Figure 1. FEROS super-spectra of TYC 8830 410 1 showing the Ca II H+K (*top*) and Li I $\lambda6708$ (*bottom*) regions. Wavelengths are in air and corrected to the heliocentric reference frame, error spectra are plotted as dotted lines. The vertical dashed line in the bottom panel indicates the expected location of Li I $\lambda6708$; no line is seen.
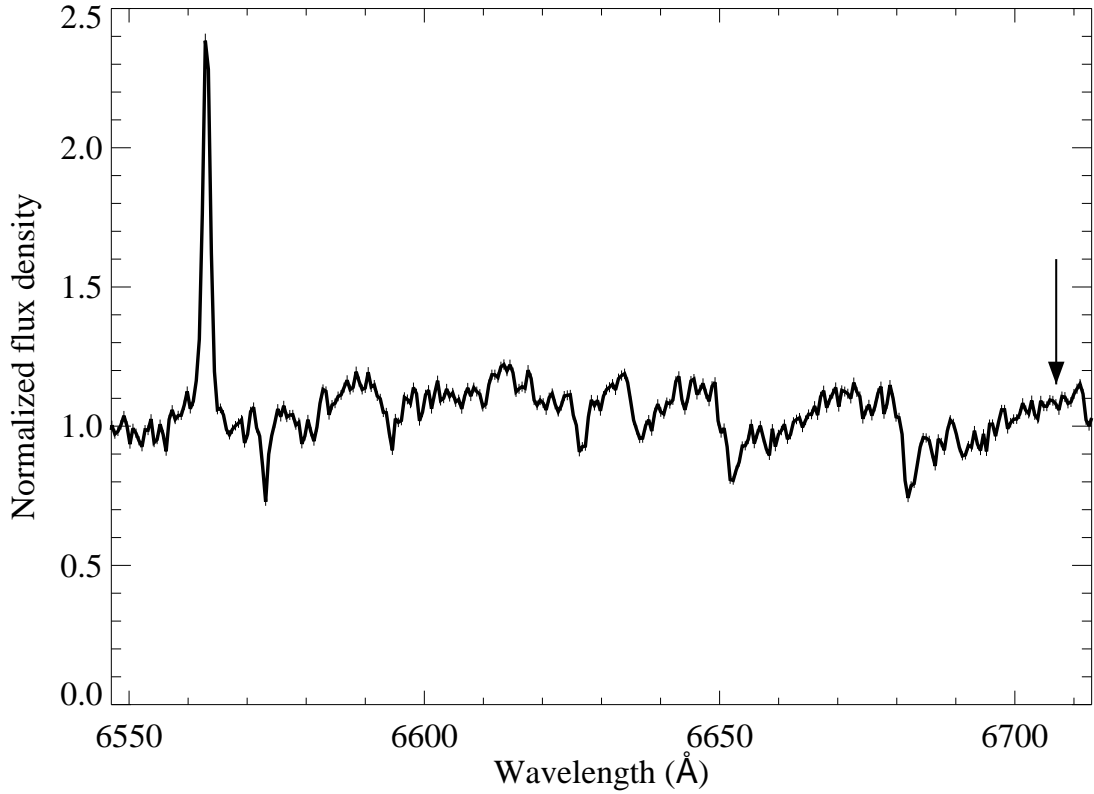
Figure 2. Segment of MagE spectra of 2MASS J2301−5858, the wide late-type companion to TYC 8830 410 1. Normalized flux per pixel and associated error (thin vertical bars) are plotted. Hα emission is evident, as well as molecular features typical of late-type stars. The downward-pointing arrow indicates the expected location of Li I λ6708; no line is seen. Equivalent widths for Hα and lithium are given in Section 4.1 while the companion spectral properties are given in Table 1.
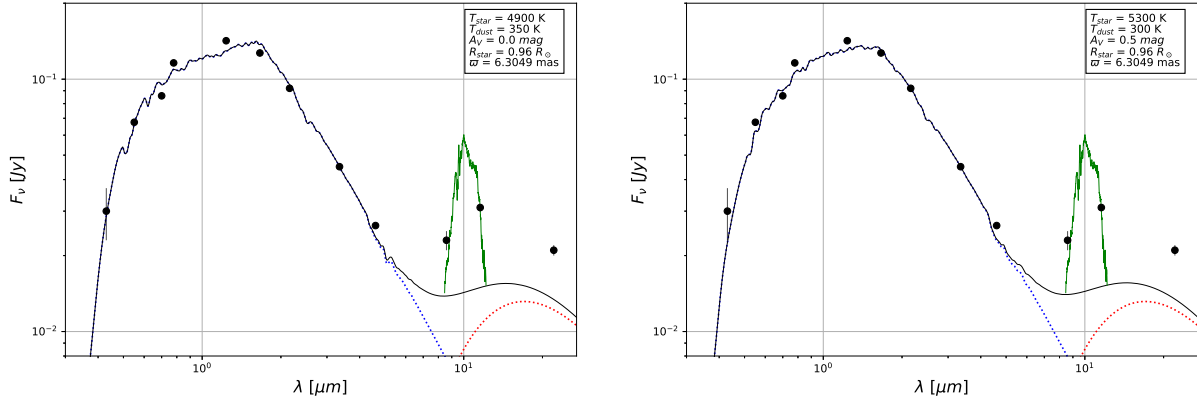
Figure 3. Spectral energy distributions for TYC 8830 410 1 for two cases: no reddening (*left*) and reddening such that A$_V$=0.5 (*right*); see discussion in Sections 4.2 and 5.1. Data points are as given in Table 3 and the green curve is the VISIR N-band spectrum. Vertical lines in data points indicate the measurement uncertainty. Some measurement uncertainties are smaller than the point sizes on the plot. The vertical scaling of the VISIR N-band spectrum is calibrated with the *WISE W*3 channel data point. The dotted blue curve connecting the *BVRIJHK*$_s$*W*1 data points is a synthetic stellar atmospheric spectrum (Hauschildt *et al.* 1999). The dotted red curve is a blackbody at the temperature indicated on the figure panel; this temperature is not well-constrained as discussed in Section 4.2. The solid black curve is the sum of the atmospheric and blackbody models.
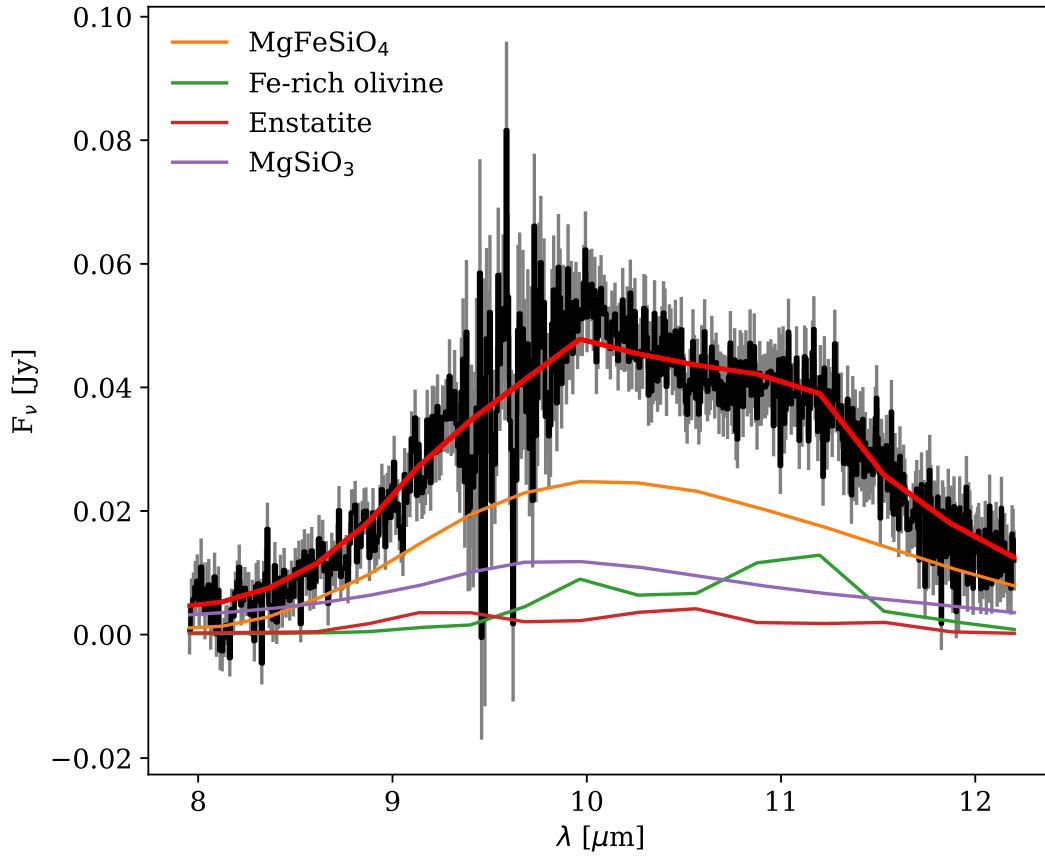
Figure 4. VISIR N-band spectrum and representative model fit (see Section 4.2 for more details). The solid black curve is the measured flux and the grey curve underneath is the associated uncertainty for each spectral sample. The red curve plotted over the data is the model fit which is the sum of the components plotted below the data and labeled in the figure legend. Fe-rich olivine (forsterite) and enstatite are crystalline species while MgFeSiO₄ and MgSiO₃ are amorphous species.
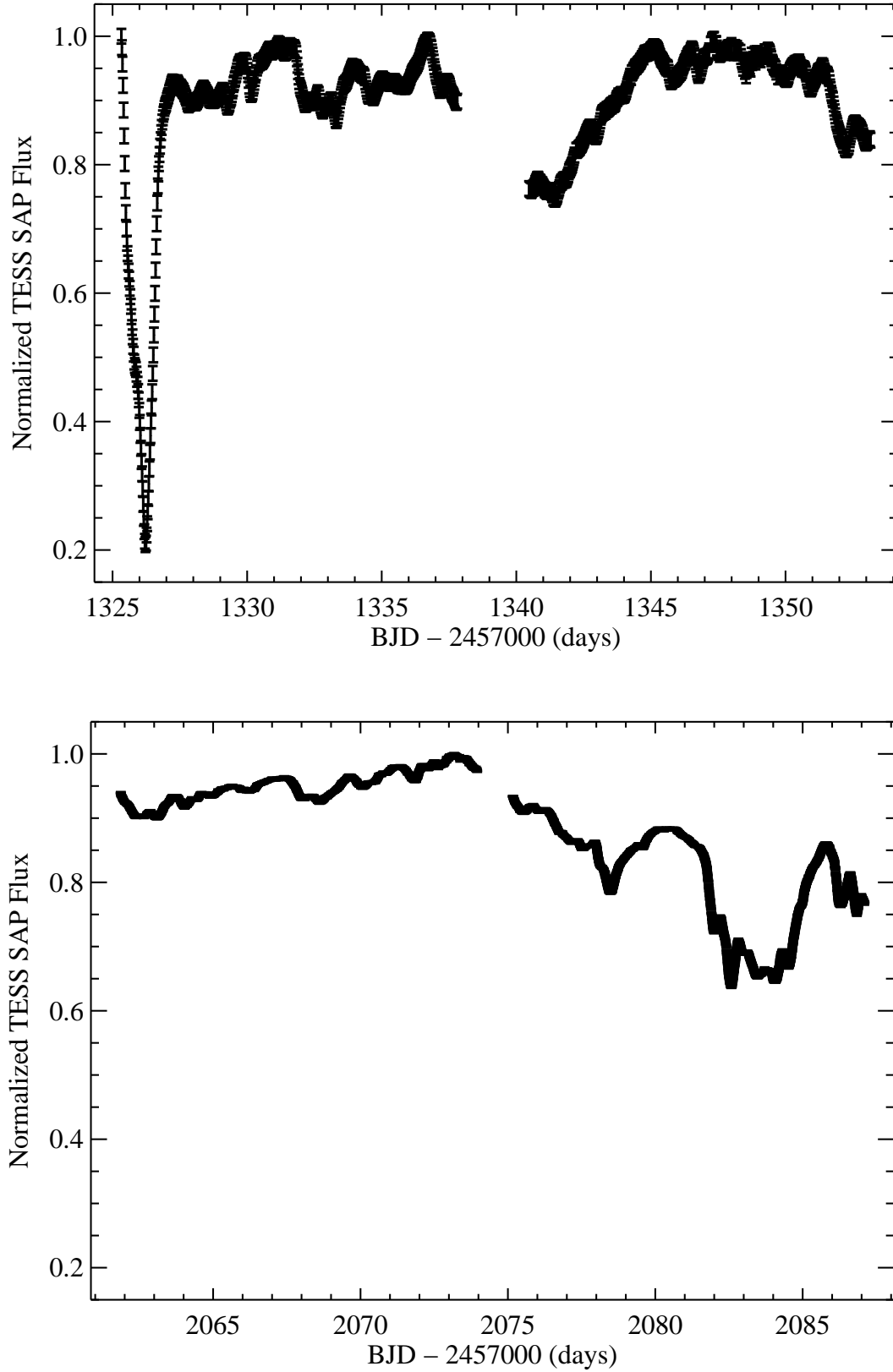
Figure 5.   *TESS* lightcurves for TYC 8830 410 1; flux is normalized to the maximum value seen in each individual panel. A deep dip and stochastic variability at the ~20% level are apparent. Each lightcurve is normalized to unity at its respective maximum value. *Top: TESS* Sector 1 FFI lightcurve. *Bottom: TESS* Sector 28 two-minute cadence lightcurve.
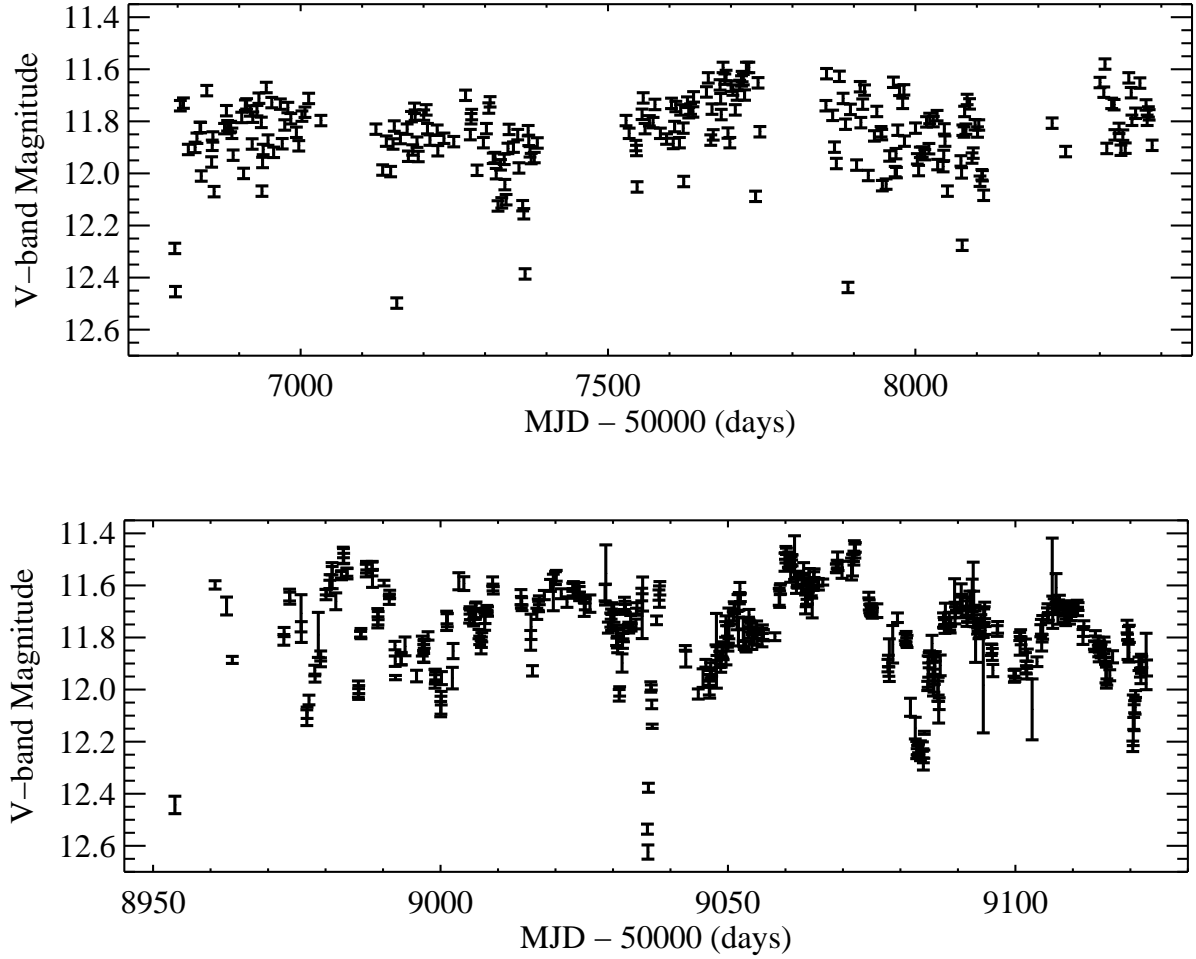
Figure 6. Ground-based optical lightcurves for TYC 8830 410 1. Several ≈1 magnitude deep dips and stochastic variability at the ~0.5 magnitude level are apparent. *Top:* ASAS-SN lightcurve. *Bottom:* LCOGT lightcurve.
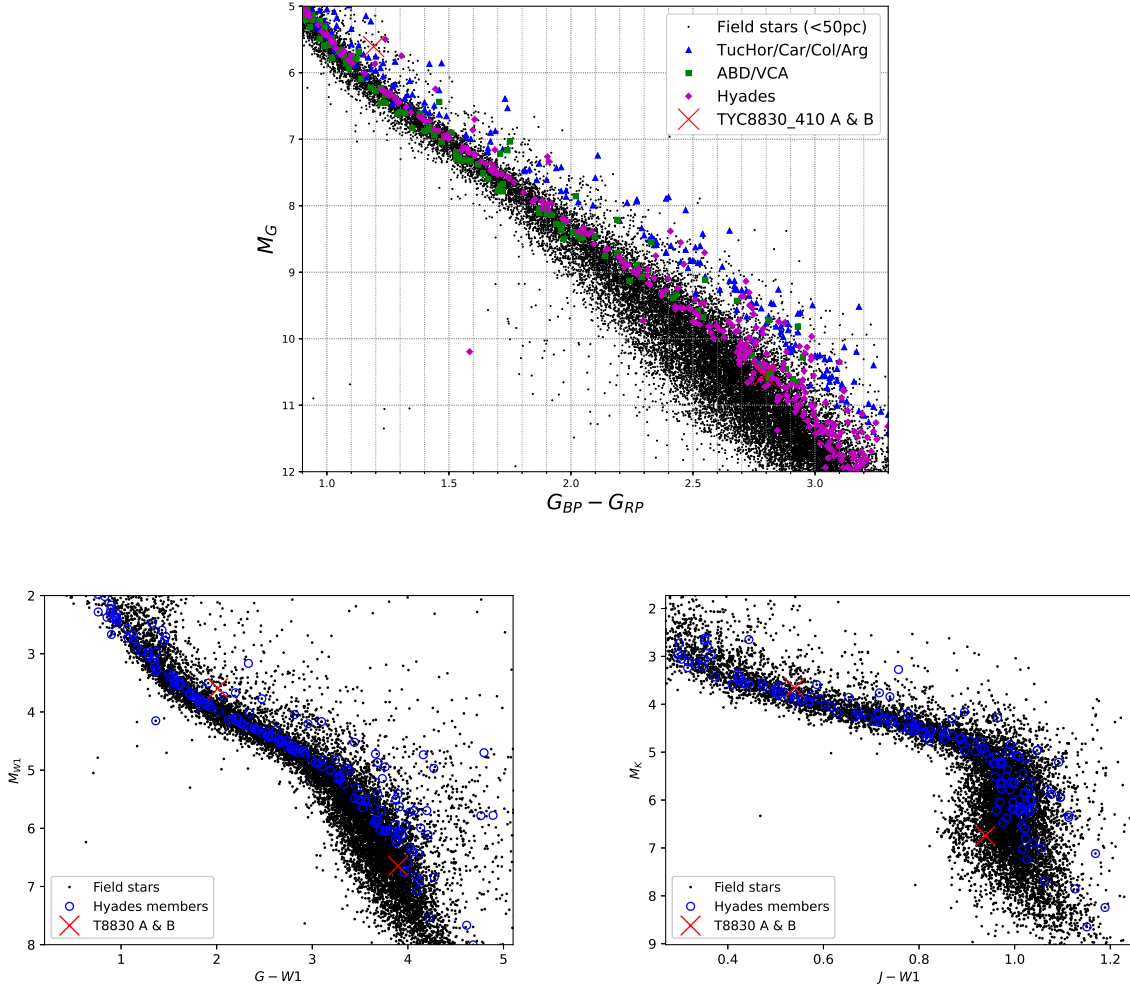
Figure 7. Color-absolute magnitude diagrams constructed from *Gaia* EDR3 photometry and parallax measurements and infrared photometry. *Top panel:* Tucana-Horologium (TucHor), Carina (Car), Columba (Col), and Argus (Arg) associations have ages of ∼30 Myr. AB Dor (ABD) and Volans-Carina (VCA) have ages of ∼100 Myr (ages from Torres *et al.* 2008; Gagné *et al.* 2018a, and references therein). *All panels:* The Hyades age is ≈680 Myr (e.g., Gossage *et al.* 2018 and references therein). TYC 8830 410 1 (TYC8830_410 A) is either ≈0.2 magnitudes too red or too luminous (or possibly some combination of both) compared to single stars of any age (unresolved, similar brightness binary systems in the Hyades are seen above the main Hyades-locus with comparable positions as TYC 8830 410 1). Given the presence of transiting dust clumps, we assume reddening is responsible for its offset position. 2MASS J2301−5858 (TYC8830_410 B) lies within the locus of Hyades mid-M dwarfs in the optical color-absolute magnitude diagram, although it may be compatible with ∼100 Myr old stars. In the infrared color-absolute magnitude diagrams it is more consistent with Hyades and field mid-M type stars within 50 pc of the Sun, which are thought to have ages on the order of gigayears.

Table 1. Stellar Parameters

Parameter	TYC 8830 410 1	2MASS J23011901−5858262
R.A. (J2016)	23 01 12.637	23 01 19.017
Decl. (J2016)	−58 58 21.74	−58 58 26.07
G_{mag}	11.60	16.54
G_{BP}−G_{RP}	1.19	2.79
Sp. Type	G9 V	M4 Ve
T_{star} (K)	5300	3300
R_{star} ($R_\odot$)	0.96	0.35
L_{star} ($L_\odot$)	0.65	0.013
pmRA (mas yr^{-1})	+27.01±0.01	+29.35±0.04
pmDE (mas yr^{-1})	−14.24±0.01	−14.71±0.04
RV (km s^{-1})	+9.9±0.1	+9.20±0.84
Parallax (mas)	6.30±0.01	6.35±0.05
Distance (pc)	158.7±0.3	157.5±1.2
UVW (km s^{-1})	−11.4±0.1, −19.1±0.1, −11.5±0.1	

NOTE— R.A. and Decl., G_{mag}, G_{BP}−G_{RP} color, proper motions (pmRA and pmDE), and parallax (and hence distance) values are from *Gaia* DR2 and EDR3 (Gaia Collaboration *et al.* 2018, 2020). Spectral types are from analysis presented in Section 4.1. T_{star} and R_{star} are extracted from atmospheric model fits to broadband photomteric measurements (e.g., Figure 3). L_{star} is then calculated using $L=4\pi R^2 \sigma_{SB} T^4$. Radial velocities are measured from our high- and medium-resolution echelle spectra. UVW space motions are reported for the primary (independent UVW space motion values for the companion are consistent but less precise) and are relative to the Sun such that positive U is towards the Galactic center, positive V is in the direction of Galactic rotation, and positive W is toward the north Galactic pole (Johnson & Soderblom 1987).

Table 2. TYC 8830 410 1 Radial Velocity Measurements

Instrument	UT Epoch	Julian Date	RV
			$(\mathrm{km\,s^{-1}})$
RAVE	2009-11-10	2455145.905162	7.0±1.8
Gaia DR2	2015	2457205.5	9.35±0.77
FEROS	2019-08-22	2458717.684903	10.012±0.014
FEROS	2019-08-25	2458720.843824	9.991±0.020
FEROS	2019-08-27	2458722.617453	9.787±0.011
FEROS	2019-08-28	2458723.702129	9.834±0.009
FEROS	2019-08-29	2458724.675237	9.875±0.010
FEROS	2019-11-13	2458800.576946	9.794±0.013
FEROS	2019-11-18	2458805.589559	9.854±0.010

NOTE—The *Gaia* DR2 measurement is a median of all epochs regardless of whether or not any variability is present; it is not yet possible to access individual epoch measurements.

Table 3. TYC 8830 410 1 Broadband Photometry

Filter Name	λ	Magnitude	Flux
	(μm)		(mJy)
B	0.43	12.85±0.25	30±7
V	0.55	11.87±0.05	67.5±0.6
R	0.70	11.34±0.05	85.9±0.8
I	0.778	10.83±0.01	116±1
J	1.235	10.13±0.02	142±3
H	1.662	9.77±0.03	127±3
$K_{\rm s}$	2.159	9.65±0.02	92±2
$W1$	3.35	9.57±0.02	45±1
$W2$	4.60	9.53±0.02	26.3±0.5
VISIR PAH1	8.59	−	23±2
$W3$	11.56	7.43±0.02	31.0±0.5
$W4$	22.09	6.51±0.06	21±1

NOTE—BVR are in the Johnson-Cousins system. B-band data are from AAVSO (Henden *et al.* 2015). V- and R-band data are converted from *Gaia* EDR3 $G_{\rm mag}$ and $G_{\rm BP}-G_{\rm RP}$ color[4]. I-band data are from DENIS (Epchtein *et al.* 1999; Fouqué *et al.* 2000), $JHK_{\rm s}$ are from 2MASS (Cutri *et al.* 2003; Skrutskie *et al.* 2006). VISIR PAH1-filter data are described in Section 3.3. $W1W2W3W4$ are from *WISE* (Cutri 2012) and are not color corrected.

APPENDIX

A. LCOGT V-BAND PHOTOMETRY FOR TYC 8830 410 1

Epoch V-band magnitudes are presented for TYC 8830 410 1 as measured with the LCOGT and described in Section 3.7. There are 484 measurements presented.

Table A1. TYC 8830 410 1 LCOGT V-band Photometric Monitoring

Modified Julian Date	V_{mag}	V_{mag} error
58953.79529	12.44	0.03
58960.78542	11.59	0.01
58962.78541	11.67	0.03
58963.78535	11.88	0.01
58972.74410	11.80	0.02
58972.78802	11.77	0.01
58973.74359	11.63	0.02
58973.78536	11.64	0.02
58975.74365	11.70	0.07
58975.78527	11.77	0.04
58976.74606	12.10	0.03
58976.78527	12.08	0.02
58977.11856	12.04	0.01
58978.11856	11.92	0.02
58978.16576	11.95	0.01
58978.74372	11.79	0.08
58979.12868	11.89	0.01
58979.16023	11.87	0.01
58980.08512	11.63	0.01
58980.11906	11.62	0.01
58980.74374	11.59	0.01
58980.78534	11.59	0.04
58981.12450	11.53	0.02
58981.16026	11.57	0.04

Table A1 *(continued)*

Modified Julian Date	V_{mag}	V_{mag} error
58981.78528	11.66	0.03
58982.74389	11.55	0.01
58982.78544	11.56	0.01
58983.07718	11.48	0.03
58983.11857	11.47	0.01
58983.16030	11.49	0.01
58983.71338	11.54	0.01
58983.74353	11.55	0.01
58985.70794	11.99	0.03
58985.74361	12.01	0.02
58985.78535	12.00	0.01
58986.08382	11.78	0.01
58986.11858	11.78	0.01
58986.16020	11.78	0.01
58987.07881	11.54	0.02
58987.11858	11.53	0.02
58987.16201	11.52	0.01
58988.07689	11.53	0.02
58988.11859	11.52	0.01
58988.16185	11.57	0.03
58989.07814	11.72	0.03
58989.11857	11.73	0.01
58989.16130	11.71	0.01
58990.17046	11.59	0.01
58991.07937	11.65	0.01
58991.11855	11.64	0.01
58991.16073	11.63	0.01
58992.07690	11.83	0.01
58992.11854	11.89	0.01
58992.16075	11.95	0.01

Table A1 *(continued)*

Modified Julian Date	V_{mag}	V_{mag} error
58993.11854	11.88	0.02
58993.16262	11.88	0.02
58993.82708	11.83	0.03
58995.82694	11.94	0.02
58996.82693	11.83	0.03
58997.04211	11.87	0.02
58997.07688	11.84	0.01
58997.11885	11.85	0.04
58997.16221	11.82	0.01
58997.82710	11.79	0.01
58999.03521	11.95	0.03
58999.07789	11.95	0.02
58999.11857	11.95	0.01
58999.16017	11.94	0.01
59000.03521	12.07	0.02
59000.07688	12.06	0.03
59000.11858	12.03	0.02
59000.16760	11.95	0.02
59001.05897	11.73	0.03
59001.12490	11.72	0.01
59001.18373	11.73	0.02
59002.06012	11.95	0.04
59002.18790	11.85	0.02
59003.18448	11.58	0.03
59004.05878	11.59	0.02
59005.05890	11.71	0.02
59005.12125	11.69	0.01
59005.18374	11.71	0.01
59005.68382	11.72	0.02
59005.74632	11.74	0.01

Table A1 *(continued)*

Modified Julian Date	V_{mag}	V_{mag} error
59005.80880	11.73	0.01
59006.05890	11.69	0.03
59006.12128	11.70	0.01
59006.18375	11.67	0.01
59006.68398	11.78	0.01
59006.80879	11.81	0.01
59007.05895	11.83	0.02
59007.12128	11.81	0.02
59007.18392	11.79	0.01
59007.68392	11.73	0.03
59007.74630	11.72	0.02
59007.81043	11.70	0.01
59008.05893	11.68	0.01
59008.12117	11.70	0.01
59008.18367	11.70	0.01
59009.05877	11.58	0.01
59009.12116	11.60	0.01
59009.18367	11.61	0.01
59013.99631	11.64	0.02
59014.05878	11.66	0.02
59014.12164	11.66	0.01
59014.18390	11.68	0.01
59015.68377	11.81	0.03
59015.74650	11.75	0.04
59015.99626	11.92	0.01
59016.74629	11.70	0.02
59016.99694	11.67	0.02
59017.06013	11.68	0.02
59017.18792	11.65	0.01
59018.05877	11.63	0.01

Table A1 *(continued)*

Modified Julian Date	V_{mag}	V_{mag} error
59019.12656	11.60	0.02
59019.62133	11.62	0.07
59020.00060	11.57	0.02
59020.12772	11.56	0.02
59020.99732	11.63	0.01
59021.99627	11.66	0.02
59022.99631	11.60	0.01
59023.06086	11.62	0.01
59023.12131	11.60	0.01
59023.18398	11.62	0.02
59023.99634	11.61	0.02
59024.05873	11.60	0.02
59024.12125	11.62	0.02
59024.18388	11.64	0.01
59024.99631	11.69	0.02
59025.05892	11.65	0.01
59025.12127	11.65	0.01
59025.18378	11.67	0.02
59025.99821	11.67	0.03
59028.62132	11.62	0.03
59028.68395	11.63	0.04
59028.74628	11.55	0.10
59029.18468	11.76	0.02
59029.62270	11.73	0.02
59029.68379	11.71	0.01
59029.74629	11.73	0.04
59029.80878	11.68	0.02
59030.12128	11.68	0.01
59030.18374	11.72	0.01
59030.62134	11.79	0.03

Table A1 *(continued)*

Modified Julian Date	V_{mag}	V_{mag} error
59030.68389	11.78	0.01
59030.74629	11.81	0.02
59030.80880	11.81	0.04
59031.07689	12.02	0.02
59031.16112	12.00	0.01
59031.58231	11.89	0.03
59031.66028	11.82	0.01
59031.74362	11.79	0.01
59031.82697	11.79	0.02
59031.99353	11.66	0.02
59032.07687	11.68	0.02
59032.16113	11.68	0.01
59032.66029	11.75	0.01
59032.74364	11.76	0.02
59033.07688	11.73	0.02
59033.16022	11.76	0.01
59033.99352	11.74	0.01
59034.07837	11.70	0.01
59034.16330	11.68	0.02
59035.00199	11.63	0.02
59035.07710	11.71	0.08
59035.16195	11.63	0.06
59035.99360	12.53	0.01
59036.08050	12.62	0.02
59036.16376	12.37	0.01
59036.57691	11.99	0.01
59036.66033	11.99	0.01
59036.74364	12.05	0.01
59036.82701	12.14	0.01
59037.57694	11.73	0.01

C. Melis *et al.*

Table A1 *(continued)*

Modified Julian Date	V_{mag}	V_{mag} error
59037.99355	11.63	0.01
59038.07688	11.64	0.04
59038.16021	11.61	0.02
59042.57700	11.84	0.01
59042.66029	11.88	0.03
59044.83058	12.01	0.01
59045.66428	11.95	0.03
59046.16020	11.89	0.01
59046.67066	11.96	0.02
59046.74698	11.99	0.02
59046.82945	12.01	0.02
59046.91588	11.94	0.01
59046.99356	11.90	0.01
59047.07689	11.93	0.01
59047.16478	11.93	0.01
59047.91151	11.85	0.02
59047.99357	11.85	0.14
59048.08371	11.85	0.01
59048.57760	11.88	0.03
59048.66029	11.87	0.02
59048.74357	11.89	0.04
59048.82694	11.89	0.02
59048.99355	11.84	0.02
59049.08345	11.85	0.02
59049.16663	11.85	0.03
59049.57810	11.76	0.02
59049.66030	11.81	0.09
59049.74361	11.78	0.03
59049.91166	11.81	0.02
59049.99357	11.84	0.01

Table A1 *(continued)*

Modified Julian Date	V_{mag}	V_{mag} error
59050.07689	11.78	0.03
59050.16019	11.74	0.05
59050.91024	11.72	0.02
59050.99571	11.71	0.02
59051.07690	11.68	0.01
59051.16020	11.68	0.01
59051.57698	11.73	0.03
59051.74434	11.66	0.03
59051.82694	11.77	0.05
59051.92056	11.66	0.03
59051.99420	11.64	0.02
59052.07697	11.61	0.02
59052.16019	11.64	0.01
59052.66294	11.76	0.04
59052.74359	11.80	0.03
59052.82695	11.83	0.01
59053.07817	11.83	0.01
59053.16017	11.83	0.02
59053.57693	11.76	0.04
59053.66031	11.71	0.01
59053.74359	11.74	0.01
59053.82703	11.74	0.01
59054.07684	11.76	0.01
59054.16018	11.81	0.02
59054.57695	11.79	0.02
59054.91240	11.78	0.01
59054.99355	11.76	0.02
59055.07697	11.80	0.02
59055.16047	11.77	0.01
59055.91177	11.80	0.03

C. Melis *et al.*

Table A1 *(continued)*

Modified Julian Date	V_{mag}	V_{mag} error
59055.99720	11.76	0.01
59056.07688	11.78	0.01
59056.16033	11.79	0.02
59058.16020	11.79	0.01
59058.91347	11.64	0.03
59058.99365	11.65	0.03
59059.07698	11.61	0.01
59059.16018	11.61	0.01
59059.91025	11.51	0.03
59059.99357	11.48	0.01
59060.07684	11.48	0.03
59060.16018	11.46	0.01
59060.50315	11.50	0.02
59060.58376	11.50	0.03
59060.91019	11.55	0.03
59060.99354	11.50	0.01
59061.07686	11.49	0.01
59061.16020	11.50	0.02
59061.57696	11.49	0.08
59061.91036	11.60	0.03
59062.00081	11.57	0.02
59062.07342	11.58	0.01
59062.15665	11.57	0.03
59062.90681	11.57	0.02
59062.99027	11.57	0.01
59063.07328	11.56	0.01
59063.16158	11.53	0.02
59063.49499	11.67	0.03
59063.58854	11.65	0.02
59063.65676	11.64	0.02

Table A1 *(continued)*

Modified Julian Date	V_{mag}	V_{mag} error
59063.74006	11.62	0.03
59063.82350	11.64	0.02
59063.90673	11.60	0.02
59063.99009	11.60	0.02
59064.07325	11.59	0.01
59064.15665	11.55	0.01
59064.49227	11.61	0.02
59064.57350	11.62	0.02
59064.65665	11.66	0.05
59064.73999	11.59	0.01
59064.82350	11.60	0.01
59064.91028	11.56	0.01
59064.99009	11.55	0.01
59065.65673	11.58	0.01
59065.73999	11.59	0.02
59066.49010	11.58	0.01
59068.84212	11.53	0.01
59068.90690	11.53	0.01
59068.99000	11.52	0.01
59069.07342	11.50	0.03
59069.15705	11.52	0.01
59069.83952	11.54	0.03
59071.49014	11.53	0.04
59071.66239	11.52	0.04
59071.83391	11.49	0.01
59071.90670	11.49	0.02
59071.99016	11.45	0.02
59072.07331	11.46	0.02
59072.15705	11.45	0.01
59074.49009	11.63	0.01

C. Melis *et al.*

Table A1 *(continued)*

Modified Julian Date	V_{mag}	V_{mag} error
59074.57339	11.67	0.01
59074.65672	11.68	0.01
59074.74009	11.69	0.01
59074.82573	11.69	0.01
59074.90665	11.70	0.01
59074.98999	11.69	0.02
59075.07333	11.71	0.01
59075.15673	11.70	0.01
59075.90708	11.69	0.02
59077.82356	11.90	0.02
59077.90690	11.89	0.02
59077.98999	11.93	0.01
59078.07348	11.88	0.08
59078.65793	11.82	0.07
59079.49009	11.72	0.01
59080.82348	11.79	0.01
59080.90667	11.80	0.02
59080.98998	11.79	0.02
59081.07331	11.81	0.01
59081.15675	11.81	0.02
59081.74596	12.06	0.03
59082.58603	12.14	0.04
59082.82332	12.23	0.03
59082.90667	12.23	0.01
59082.98998	12.23	0.01
59083.07330	12.23	0.02
59083.15676	12.22	0.01
59083.49088	12.23	0.03
59083.82336	12.21	0.01
59083.90665	12.24	0.01

Table A1 *(continued)*

Modified Julian Date	V_{mag}	V_{mag} error
59083.99001	12.29	0.01
59084.07336	12.24	0.01
59084.15668	12.16	0.01
59084.74004	11.98	0.01
59084.82337	11.93	0.06
59084.90662	11.92	0.02
59084.98997	11.88	0.02
59085.07331	11.86	0.01
59085.49165	11.82	0.03
59085.57494	11.87	0.01
59085.66036	11.93	0.01
59085.74382	11.98	0.04
59085.82334	11.98	0.02
59085.90664	11.92	0.05
59085.98997	11.91	0.03
59086.07331	11.87	0.01
59086.49216	12.00	0.03
59086.57541	11.98	0.03
59086.65878	12.08	0.04
59086.74202	12.05	0.02
59086.92207	11.90	0.03
59087.49020	11.73	0.02
59087.57343	11.74	0.02
59087.65901	11.74	0.01
59087.74235	11.76	0.01
59087.82315	11.71	0.04
59087.90870	11.74	0.01
59088.49016	11.73	0.03
59088.57607	11.75	0.01
59088.65941	11.77	0.01

Table A1 *(continued)*

Modified Julian Date	V_{mag}	V_{mag} error
59088.74276	11.74	0.01
59089.42410	11.63	0.06
59089.49013	11.70	0.04
59089.57661	11.70	0.01
59089.65978	11.68	0.01
59089.74359	11.68	0.01
59090.42128	11.66	0.02
59090.49002	11.66	0.02
59090.57348	11.64	0.04
59090.66012	11.66	0.02
59090.74876	11.68	0.04
59091.41853	11.69	0.01
59091.49012	11.69	0.03
59091.57334	11.70	0.05
59091.66083	11.72	0.01
59091.74007	11.71	0.02
59092.07327	11.65	0.03
59092.41580	11.70	0.01
59092.49008	11.63	0.06
59092.65669	11.61	0.10
59092.74005	11.69	0.06
59093.00037	11.68	0.01
59093.07600	11.82	0.06
59093.41311	11.77	0.01
59093.49007	11.75	0.01
59093.57344	11.76	0.02
59093.65669	11.77	0.03
59093.74066	11.76	0.03
59093.99016	11.73	0.01
59094.41169	11.98	0.18

Table A1 *(continued)*

Modified Julian Date	V_{mag}	V_{mag} error
59094.49008	11.72	0.03
59094.57356	11.71	0.03
59094.65677	11.69	0.03
59094.74014	11.77	0.01
59095.82404	11.84	0.02
59095.90681	11.84	0.01
59095.98997	11.86	0.02
59096.07683	11.92	0.02
59096.82825	11.77	0.02
59096.90670	11.76	0.02
59099.75746	11.93	0.01
59099.82332	11.94	0.02
59099.90665	11.94	0.02
59099.98996	11.93	0.01
59100.75474	11.79	0.01
59100.82334	11.83	0.03
59100.91616	11.78	0.01
59100.98998	11.81	0.01
59101.75390	11.83	0.02
59101.82336	11.91	0.02
59101.90668	11.92	0.01
59101.99004	11.93	0.02
59102.07830	11.86	0.02
59102.90641	12.07	0.11
59103.74648	11.89	0.01
59104.41184	11.77	0.02
59104.50743	11.75	0.02
59104.57339	11.82	0.03
59104.65673	11.80	0.01
59104.74020	11.76	0.04

Table A1 *(continued)*

Modified Julian Date	V_{mag}	V_{mag} error
59105.57349	11.71	0.02
59105.65672	11.69	0.01
59105.74007	11.71	0.01
59106.40806	11.56	0.14
59106.49005	11.70	0.06
59106.57337	11.69	0.01
59106.74227	11.66	0.01
59107.07339	11.60	0.05
59107.40669	11.71	0.03
59107.49002	11.68	0.02
59107.57336	11.67	0.01
59107.65678	11.65	0.01
59108.40677	11.69	0.01
59108.49005	11.68	0.02
59108.57338	11.73	0.01
59108.65674	11.69	0.01
59108.74015	11.72	0.03
59108.82348	11.71	0.01
59109.41375	11.70	0.03
59109.49002	11.67	0.01
59109.58051	11.69	0.01
59109.65677	11.69	0.02
59109.73981	11.70	0.03
59109.83319	11.69	0.01
59109.90663	11.67	0.01
59110.74702	11.67	0.01
59110.82351	11.70	0.01
59110.91291	11.68	0.01
59111.74676	11.79	0.02
59111.82333	11.77	0.01

Table A1 *(continued)*

Modified Julian Date	V_{mag}	V_{mag} error
59111.90663	11.74	0.01
59113.74000	11.82	0.01
59113.82330	11.83	0.01
59113.90664	11.78	0.01
59114.40678	11.81	0.01
59114.49004	11.85	0.01
59114.57341	11.87	0.01
59114.65677	11.83	0.02
59114.74010	11.84	0.02
59114.82331	11.85	0.01
59114.90664	11.85	0.02
59115.40673	11.83	0.03
59115.49003	11.84	0.03
59115.57338	11.86	0.02
59115.65703	11.88	0.01
59115.74001	11.93	0.03
59115.82325	11.95	0.04
59115.90664	11.97	0.01
59116.41185	11.94	0.02
59116.90670	11.87	0.02
59119.42069	11.75	0.02
59119.49857	11.79	0.01
59119.57340	11.84	0.03
59119.65697	11.79	0.03
59119.74015	11.85	0.03
59119.82336	11.78	0.03
59120.41186	12.21	0.02
59120.49116	12.11	0.09
59120.57340	12.13	0.02
59120.65957	12.10	0.04

C. Melis *et al.*

Table A1 *(continued)*

Modified Julian Date	V_{mag}	V_{mag} error
59120.74000	12.06	0.02
59120.82332	12.06	0.02
59120.90663	12.01	0.01
59121.49022	11.90	0.02
59121.74004	11.93	0.01
59121.82338	11.93	0.04
59121.90676	11.90	0.03
59121.98995	11.89	0.02
59122.73995	11.89	0.10
59122.82330	11.91	0.03